

Perfect remote quantum state transfer in a superconducting qubit chain with parametrically tunable couplings

X. Li,^{1,*} Y. Ma,^{1,*} J. Han,¹ Tao Chen,² Y. Xu,¹ W. Cai,¹ H. Wang,¹
Y. P. Song,¹ Zheng-Yuan Xue,^{2,†} Zhang-qi Yin,^{1,‡} and Luyan Sun^{1,§}

¹Center for Quantum Information, Institute for Interdisciplinary Information Sciences, Tsinghua University, Beijing 100084, China

²Guangdong Provincial Key Laboratory of Quantum Engineering and Quantum Materials, and School of Physics and Telecommunication Engineering, South China Normal University, Guangzhou 510006, China

Faithfully transferring quantum state is essential for quantum information processing. Here, we demonstrate a fast (in 84 ns) and high-fidelity (99.2%) quantum state transfer in a chain of four superconducting qubits with nearest-neighbor coupling. This transfer relies on full control of the effective couplings between neighboring qubits, which is realized only by parametrically modulating the qubits without increasing circuit complexity. Once the couplings between qubits fulfill specific ratio, a perfect quantum state transfer can be achieved in a single step, therefore robust to noise and accumulation of experimental errors. This quantum state transfer can be extended to a larger qubit chain and thus adds a desirable tool for future quantum information processing. The demonstrated flexibility of the coupling tunability is suitable for quantum simulation of many-body physics which requires different configurations of qubit couplings.

High-fidelity quantum state transfer (QST) from one place to another is important for both quantum communication and scalable quantum computation [1]. Long distance QST is an essential element for quantum network [2], which requires high-efficient interfaces for transferring stationary quantum states to flying photonic qubits [3–7]. On the other hand, short distance QST is important for on-chip quantum information processing, such as communication among quantum processors and writing (reading) quantum information into (out) quantum memories [8]. To achieve short distance QST, which is our main focus, previous methods include physically moving the qubits holding quantum information to other target sites [9]. However, solid-state qubits are usually static and coupled with each other. Therefore, it is desired to realize QST in such systems solely through the interactions between qubits. This goal could be achieved by a sequential SWAP operations between nearest neighbors through active control of the qubits, but this method will accumulate individual operation errors.

Alternatively, QST in a qubit chain can be realized in a single step [10–16], which eliminates the error accumulation problem. In particular, a perfect QST in an arbitrarily long chain was proposed in Ref. 11 without active qubit control when the coupling strengths between the qubits fulfill specific conditions. Since then, the perfect QST protocol [11] has been demonstrated in nuclear magnetic resonance [17] and optical systems [18, 19]. However, it is challenging to realize this protocol in solid-state quantum systems because it is typically difficult to precisely preset the couplings among qubits for variable lengths of QST. Therefore, to meet the perfect QST condition [11], tunable coupling between qubits is necessary. Moreover, this tunability is also of particular importance for realizing two-qubit quantum gates [20–23]. However, the coupling tunability usually comes at the cost of additional decoherence or circuit complexity [24–29].

In this work, we adopt a method of parametrical modulation of qubit frequencies to realize tunable qubit coupling strengths [30–34] and experimentally demonstrate a perfect

QST in a chain of four coupled superconducting transmon qubits. In this method, the modulating fields provide control over qubit-qubit interactions without relying on extra coupling elements, and thus the circuit complexity remains the simplest. In our experiment, we first realize a large-range tunable coupling between two nearest-neighbor qubits by parametrically modulating only one qubit. We next verify the coupling strength tunability for a chain with multiple modulations, where the qubits in the middle are affected by multiple fields. Finally, we apply this technique to a chain with four qubits and experimentally realize a QST in 84 ns with a fidelity of 99.2%, characterized by quantum process tomography. The demonstrated flexibility of the coupling tunability can be further applied to quantum simulation experiments [35, 36], which require different configurations of qubit coupling strengths.

We first briefly discuss how to tune the coupling strengths in a one-dimensional chain consisting of N capacitively coupled qubits, as shown in Fig. 1a. The system Hamiltonian can be described by

$$H/\hbar = \sum_{j=0}^{N-1} \frac{\omega_j}{2} \sigma_j^z + \sum_{j=1}^{N-1} g_j (\sigma_{j-1}^+ + \sigma_{j-1}^-) (\sigma_j^+ + \sigma_j^-), \quad (1)$$

where σ_j^{\pm} are the Pauli operators on the j th qubit Q_j with a transition frequency ω_j , and g_j is the static coupling strength between qubits Q_{j-1} and Q_j . Full tunability of the coupling strength can be achieved by parametrically modulating the qubits, i.e., each Q_j with $1 \leq j \leq N-1$ is biased by an ac magnetic flux to periodically modulate its frequency as

$$\omega_j = \omega_{0j} + \varepsilon_j \sin(\nu_j t + \varphi_j), \quad (2)$$

where ω_{0j} is the mean operating frequency, ε_j , ν_j , and φ_j are the modulation amplitude, frequency, and phase, respectively. As the first qubit is not modulated, $\omega_0 = \omega_{00}$. Neglecting the higher order oscillating terms, when $\Delta_j = \omega_{0j} - \omega_{0(j-1)}$ equals to ν_j ($-\nu_j$) for odd (even) j , we get a chain of qubits

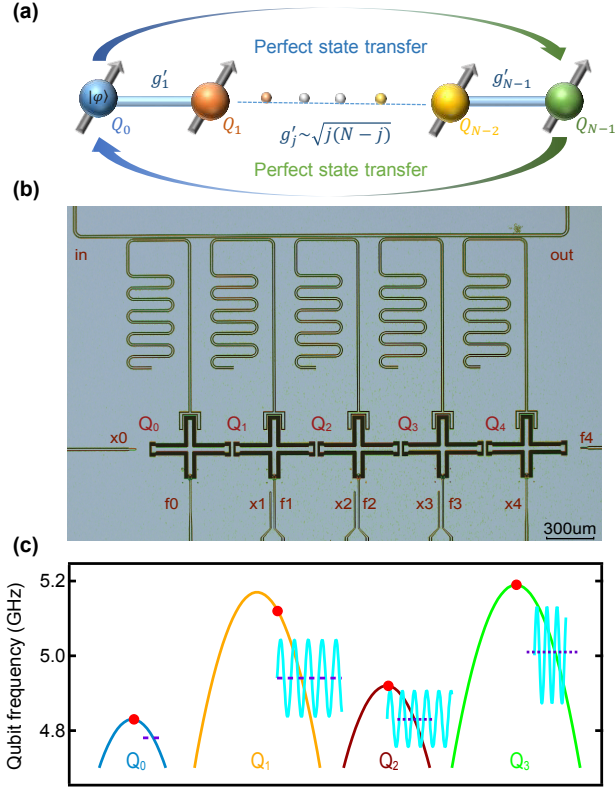


FIG. 1: **(a) Perfect remote QST.** The quantum state is transferred from the first qubit Q_0 to the last qubit Q_{N-1} in a chain when the couplings between neighboring qubits satisfy specific ratio. **(b) The five-qubit chain sample.** Five cross-shaped transmon qubits ($Xmons$, $Q_0 - Q_4$) arranged in a linear array. Each qubit has independent XY and Z control (labelled as “ x ” and “ f ” respectively), and is coupled to a separate $\lambda/4$ resonator for simultaneous and individual readout. **(c) Schematic of the operating regime for a QST from Q_0 to Q_3 with Q_4 being decoupled.** Both state preparation and measurement of each qubit are performed at the red points (the idle points) which are the maximum frequency spots (sweet spots) with the best coherence times for Q_0, Q_2 , and Q_3 . Q_1 is biased about 60 MHz below its sweet spot to avoid the unwanted crosstalk between Q_1 and Q_3 . The dashed line (the “operating” point) represents the mean operating frequency of each qubit during the QST experiment: for Q_0 , it is fixed at the dashed line; for $Q_1 - Q_3$, their frequencies are parametrically modulated around the dashed lines to achieve the required coupling g'_j between neighboring qubits.

with the nearest-neighbor resonant XY coupling in the interaction picture. Then the effective Hamiltonian [37] is

$$H_I/\hbar = \sum_{j=1}^{N-1} g'_j \sigma_{j-1}^+ \sigma_j^- + \text{H.c.}, \quad (3)$$

where the effective coupling strength

$$g'_j = g_j J_1(\alpha_j) \times \begin{cases} e^{i(\varphi_1 + \pi/2)}, & j = 1; \\ J_0(\alpha_{j-1}) e^{-i(\varphi_j - \pi/2)}, & j \text{ is even}; \\ J_0(\alpha_{j-1}) e^{i(\varphi_j + \pi/2)}, & j \text{ is odd and } \neq 1, \end{cases} \quad (4)$$

with $J_m(\alpha)$ being the m th Bessel function of the first kind.

g'_j can be conveniently tuned via changing $\alpha_j = \varepsilon_j/v_j$ of the external modulation.

With a wide range tunability of the coupling strength in hand, we now turn to the demonstration of a perfect QST along a chain of qubits [11]. Initially, we prepare the i th qubit Q_i in state $|\psi_i\rangle = \alpha|g\rangle + \beta|e\rangle$, and all other qubits are in the ground state $|g\rangle$ ($|e\rangle$ represents the excited state). In order to realize a perfect QST, the coupling strengths need to fulfill the relation $g'_j = g' \sqrt{j(N-j)}$ [11], where g' is a constant. When the system evolves under the Hamiltonian in Eq. (3) for a specific time $\tau = \pi/(2g')$, a perfect QST is achieved, such that qubit Q_{N-1-i} is in the state $|\psi_{N-1-i}\rangle = |\psi_i\rangle$ while all other qubits are back to $|g\rangle$. In our experiment, we demonstrate the case of $N = 4$ and $i = 0$.

Our experiment is implemented with a superconducting circuit [38–40], where five cross-shaped transmon qubits ($Xmons$, $Q_0 - Q_4$) [23, 41, 42] are arranged in a linear array with nearly identical nearest-neighbor coupling strengths $g/2\pi \approx 17$ MHz, as shown in Fig. 1b. Each qubit has independent XY and Z control and is coupled to a separate $\lambda/4$ resonator for simultaneous and individual readout. The qubits have averaged $T_1 \approx 22 \mu\text{s}$ and $T_2^* \approx 19 \mu\text{s}$ at the flux sweet spots. A Josephson parametric amplifier [43–46] with a gain over 20 dB and a bandwidth about 260 MHz is used for high-fidelity single-shot measurements of the qubits. Meanwhile, we use a calibration matrix to reconstruct the readout results for a better indication of the qubit state. Experimental setup, readout properties, and device parameters are all presented in Ref. 37.

As a demonstration, we use the first four qubits ($Q_0 - Q_3$) to realize the QST, while biasing Q_4 at a low frequency (< 4 GHz) which is nearly completely decoupled from the first four qubits. Synchronization and phase stability of both XY and Z controls are critical for a high-fidelity QST. Therefore, in our experiment, we use two synchronized four-channel arbitrary waveform generators to fully manipulate the four qubits. Figure 1c shows the biasing and operating regime of the four qubits. Both state preparation and final measurement of each qubit are performed at or near the maximum frequency spot (the idle point at ω_{s_j} with $j = 0, 1, 2, 3$) with the best coherence times. During the QST experiment, all qubits are pulsed to the “operating” points, ω_{o_j} . While Q_0 stays fixed, the other three qubits are parametrically driven to oscillate sinusoidally around their operating points to achieve the required coupling g'_j between neighboring qubits.

We first demonstrate the tunability of g'_j by parametric modulations of the transition frequencies of the qubits. There are two scenarios of tuning g'_j : one qubit is modulated while the other one remains at a fixed frequency; both qubits are modulated simultaneously. The former case of parametric modulation has been used to create entangling gates between two transmon qubits [33, 34, 47]. However, to our knowledge the latter case with simultaneous parametric modulations on two qubits has not yet been demonstrated experimentally. Figures 2a and 2b show the experimental results of the two scenarios respectively, demonstrating smooth and full control

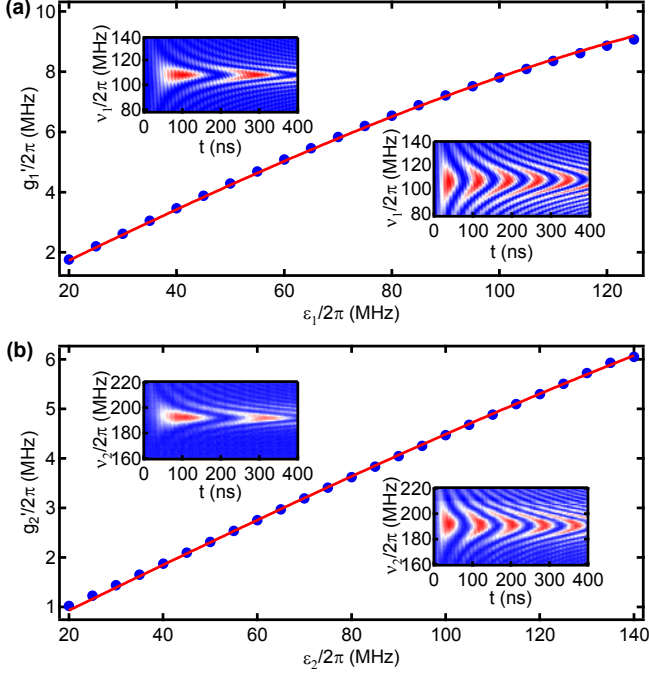


FIG. 2: **(a) Tunable coupling g'_1 between Q_0 and Q_1 as a function of ε_1 with other qubits being decoupled.** g'_1 is extracted from the so-called “chevron” pattern. Q_0 is prepared in $|e\rangle$ and biased at a fixed point ω_{00} , while Q_1 , initially in $|g\rangle$, is flux biased to oscillate sinusoidally as $\omega_1 = \omega_{01} + \varepsilon_1 \sin(\nu_1 t + \varphi_1)$. Coherent excitation oscillation between Q_0 and Q_1 as a function of ν_1 and time t at fixed ε_1 produces a chevron pattern. The full scale oscillation is achieved when $\nu_1 = \Delta_1 = \omega_{01} - \omega_{00}$ and its oscillation frequency gives the effective coupling g'_1 (dots). Two typical chevron patterns are shown in the inset with blue and red colors corresponding to $|g\rangle$ and $|e\rangle$ of Q_1 respectively: top-left and bottom-right ones correspond to $\varepsilon_1/2\pi = 30$ MHz and $\varepsilon_1/2\pi = 80$ MHz, respectively. **(b) Tunable coupling g'_2 between Q_1 and Q_2 as a function of ε_2 with other qubits being decoupled.** Both Q_1 (initially in $|e\rangle$) and Q_2 (initially in $|g\rangle$) are parametrically driven as $\omega_1 = \omega_{01} + \varepsilon_1 \sin(\nu_1 t + \varphi_1)$ and $\omega_2 = \omega_{02} + \varepsilon_2 \sin(\nu_2 t + \varphi_2)$ simultaneously. Similarly, at $\nu_2 = \Delta_2 = \omega_{02} - \omega_{01}$, the oscillation frequency gives the effective coupling g'_2 (dots). The top-left and bottom-right insets show the chevron pattern with $\varepsilon_2/2\pi = 50$ MHz and $\varepsilon_2/2\pi = 140$ MHz, respectively. The red lines in both (a) and (b) are fitted with Eq. (4). The resulting $g_1/2\pi \approx g_2/2\pi \approx 19$ MHz is slightly larger than the one measured from a static case in which the chevron pattern is measured while tuning the frequency of one qubit across the other with no parametric modulation. The deviation is presumably due to imperfect deconvolution [37] of the flux pulse so the effective ε_1 and ε_2 are slightly larger than applied.

of g'_j as a function of ε_j .

Once proper g'_j s between neighboring qubits in the chain are achieved by appropriate qubit frequency modulations, perfect QST can be calibrated by measuring the population of each qubit as a function of time. Figure 3a shows the experimental sequence. Initially, all four qubits are at their idle points and in the ground state except for Q_0 prepared in the excited state. Then step pulses are utilized to change the qubits from their idle spots to the operating points. $Q_1 - Q_3$ are fre-

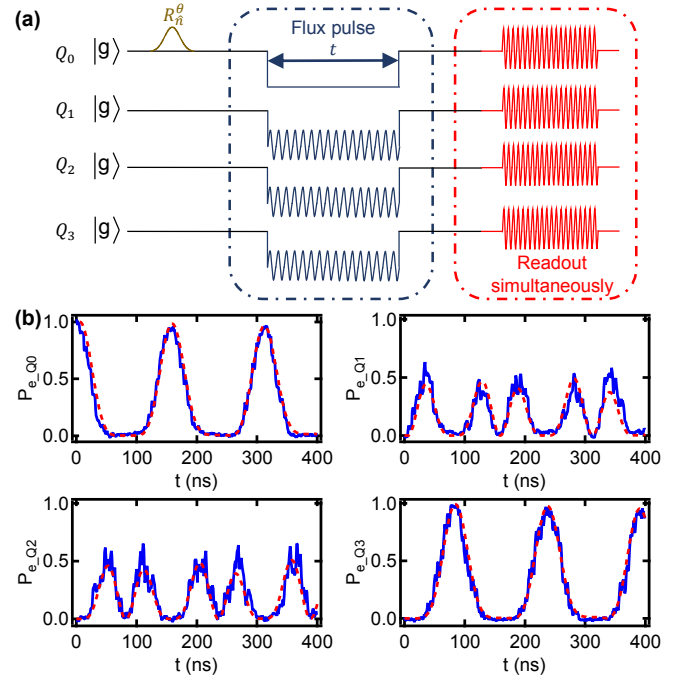


FIG. 3: **(a) Experimental sequence for QST.** Initially, all four qubits are at their idle points with only Q_0 prepared in an arbitrary state by R_n^0 . Then step pulses are utilized to change the qubits from their idle spots to the operating points. $Q_1 - Q_3$ are modulated to achieve the required coupling ratio for a perfect QST. The operation is on for various time t , followed by step pulses to return all qubits back to their idle points for the final qubit state readout. **(b) Time evolution of the qubit excited state populations.** The populations are measured simultaneously at different t for the case with Q_0 initially in $|e\rangle$. The red dashed lines are numerically simulated results with the measured parameters based on Hamiltonian in Eq. (3). The population evolutions of Q_1 and Q_2 are noisier because in our implementation Q_1 and Q_2 are affected by multiple modulations which lead to more high-order oscillations and crosstalk. The slight deviation between simulation and experiment mainly comes from the high-order terms and imperfect readout calibration matrix due to the unwanted crosstalk between qubits. At $t = 84$ ns, a QST from Q_0 to Q_3 is achieved.

quency modulated with the calibrated ε 's and ν 's such that $g'_1 : g'_2 : g'_3 = \sqrt{3} : 2 : \sqrt{3}$ as required for a perfect QST [11]. The operation is on for various time t , followed by step pulses as well to return all qubits to their idle points for the final state readout. Figure 3b shows the measured qubit populations as a function of time. As expected, the population of Q_0 first spreads to Q_1 , Q_2 , and Q_3 . At $t = 84$ ns, the population is transferred to Q_3 while all Q_0 , Q_1 , and Q_2 go back to the ground states, realizing a fast and nearly perfect QST. As t becomes longer, the reverse process occurs. At $t = 168$ ns, the population of Q_3 is transferred back to Q_0 . This transfer can keep going back and forth as t increases. As will be shown below, this property allows us to better calibrate the QST's process fidelity with repeated transfers. This way of calibration can eliminate the detrimental effect in the “round trip” of the qubit frequency between the idle and operating points, and

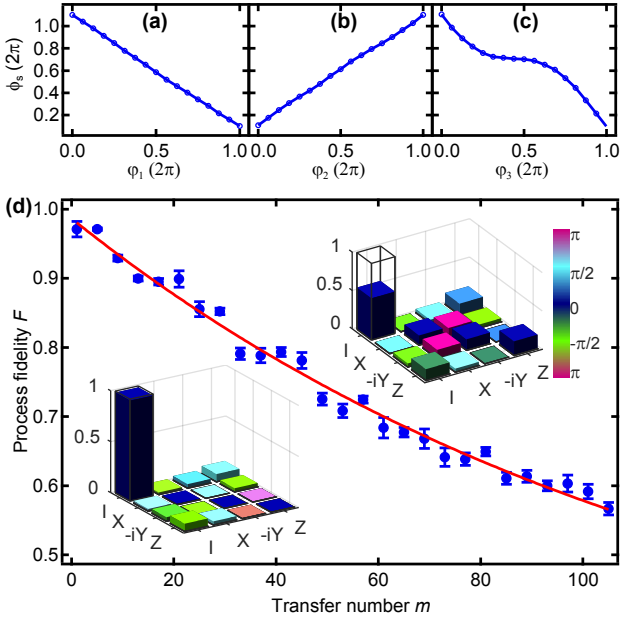


FIG. 4: (a-c) **Dependence of phase ϕ_s of the transferred state on ϕ_1 , ϕ_2 , and ϕ_3 of the modulation pulses.** The dependence of ϕ_s on ϕ_1 and ϕ_2 are linear but with opposite slopes as expected. The dependence of ϕ_s on ϕ_3 deviates from a linear curve due to an extra phase accumulation. (d) **QST process fidelity.** Process tomography is used to benchmark the QST performance and is plotted as a function of the number of transfers, which is controlled by setting the operating times $t = (4n + 1) \times 84$ ns, equivalent to perform 1, 5, 9, \dots transfer processes. The phase of the transferred state on Q_3 is deterministic and can be well controlled by adjusting the phases in the sinusoidal modulation pulses as shown in a-c. The presented process fidelities are all based on the transferred states after proper phase adjustments. The parameters ε_i and v_i ($i = 1, 2, 3$) are critical for a high-fidelity QST and thus are further optimized by the function “fminsearch” in Matlab. Each point is averaged 10,000 times and the error bars corresponding to one standard deviation are obtained from 10 repeated experiments. The red curve is a fit based on $F = AP^m + 0.25$ with $A = 0.737$ and $P = 0.992$, demonstrating a nearly perfect QST. The bottom-left (top-right) inset shows the χ matrix after 1 (105) QST. The bar height and color correspond to the amplitude and phase of the χ matrix element, respectively.

only focus on the accumulation of errors during the transfer.

The phase of the transferred state ϕ_s depends on the three phases ϕ_1 , ϕ_2 , and ϕ_3 of the parametric modulations as shown in Figs. 4a-c, where ϕ ’s are the phases in the corresponding sinusoidal flux drives. ϕ_s is a linear function of ϕ_1 and ϕ_2 as expected from Eq. (4). However, the dependence of ϕ_s on ϕ_3 deviates from the expected linear curve. This is because ϕ_s also includes an extra phase accumulation during Q_3 ’s frequency modulation when ϕ_3 changes. Nevertheless, ϕ_s can be fully controlled by ϕ_1 , ϕ_2 , and ϕ_3 individually.

Quantum process tomography [8, 37, 48] is used to benchmark the QST performance and the fidelity is defined as the overlap between χ_M and χ_{ideal} (χ_{ideal} is for a perfect QST) $F = \text{tr}(\chi_M \chi_{\text{ideal}})$, where χ_M is the derived 4×4 process ma-

trix for the experimental operation. Figure 4d shows the measured process fidelity as a function of the number of transfers. The number of transfers is controlled by properly setting the operating time. A fit (red curve) based on $F = AP^m + 0.25$ gives $A = 0.737$ and $P = 0.992$, demonstrating a nearly perfect QST. This high-fidelity process is possible mainly because the fast QST approach requires only a single step, which minimizes the qubit decoherence effect and is robust to noise and accumulation of experimental errors. We note that the pure dephasing time of the transferred state in the QST is much longer than the average dephasing time of individual qubits at the operating points, and it implies the collective dynamical process provides additional coherence protection.

In conclusion, we have demonstrated a fast and high-fidelity QST with four superconducting qubits arranged in an array with nearest-neighbor coupling. This transfer relies on full control of the effective couplings between neighboring qubits by parametrically modulating the qubits. This tunable technique can be extended to a much larger system and importantly the transfer can be achieved in a single step, thus robust to noise and accumulation of experimental errors. The coupling tunability can be realized in-situ without increasing the circuit complexity, therefore provides a powerful and desirable tool for future quantum information processing.

Our experiment can be easily extended to achieve entanglement distribution between remote qubits in a chain [19]. Our technique can also be directly generalized to study the topologically-protected QST from one end to another [49], which requires different configurations of the coupling strengths. In addition, our scheme can be generalized to two-dimensional lattice scenario, where the tunable amplitudes and phases of the coupling strengths allow for quantum simulation of lattice models [36, 50].

Z.Y.X. and T.C. are supported in part by the National Key R&D Program of China (Grant No. 2016YFA0301803). Z.Q.Y. acknowledges the support from National Natural Science Foundation of China Grant No. 61771278. LS acknowledges the support from National Natural Science Foundation of China Grant No.11474177, National Key Research and Development Program of China No.2017YFA0304303, and the Thousand Youth Fellowship program in China.

* These two authors contributed equally to this work.

† Electronic address: zyxue83@163.com

‡ Electronic address: yinzhangqi@tsinghua.edu.cn

§ Electronic address: luyansun@tsinghua.edu.cn

[1] D. P. Divincenzo, Fortsch. Phys. **48**, 771 (2000).

[2] H. J. Kimble, Nature **453**, 1023 (2008).

[3] J. I. Cirac, P. Zoller, H. J. Kimble, and H. Mabuchi, Phys. Rev. Lett. **78**, 3221 (1997).

[4] A. Serafini, S. Mancini, and S. Bose, Phys. Rev. Lett. **96**, 010503 (2006).

[5] Z.-q. Yin and F.-l. Li, Phys. Rev. A **75**, 012324 (2007).

- [6] C. Axline, L. Burkhardt, W. Pfaff, M. Zhang, K. Chou, P. Campagne-Ibarcq, P. Reinhold, L. Frunzio, S. M. Girvin, L. Jiang, et al., *Nat. Phys.* DOI:10.1038/s41567-018-0115-y (2018).
- [7] P. Kurpiers, P. Magnard, T. Walter, B. Royer, M. Pechal, J. Heinsoo, Y. Salathé, A. Akin, S. Storz, J.-C. Besse, et al., arXiv:1712.08593 (2017).
- [8] M. A. Nielsen and I. L. Chuang, *Quantum Computation and Quantum Information* (Cambridge Univ. Press, 2000).
- [9] D. Kielpinski, C. Monroe, and D. J. Wineland, *Nature* **417**, 709 (2002).
- [10] S. Bose, *Phys. Rev. Lett.* **91**, 207901 (2003).
- [11] M. Christandl, N. Datta, A. Ekert, and A. J. Landahl, *Phys. Rev. Lett.* **92**, 187902 (2004).
- [12] A. Romito, R. Fazio, and C. Bruder, *Phys. Rev. B* **71**, 100501 (2005).
- [13] T. Shi, Y. Li, Z. Song, and C.-P. Sun, *Phys. Rev. A* **71**, 032309 (2005).
- [14] S. Bose, *Contemp. Phys.* **48**, 13 (2007).
- [15] C. Di Franco, M. Paternostro, and M. Kim, *Phys. Rev. Lett.* **101**, 230502 (2008).
- [16] N. Y. Yao, L. Jiang, A. V. Gorshkov, Z.-X. Gong, A. Zhai, L.-M. Duan, and M. D. Lukin, *Phys. Rev. Lett.* **106**, 040505 (2011).
- [17] J. Zhang, G. L. Long, W. Zhang, Z. Deng, W. Liu, and Z. Lu, *Phys. Rev. A* **72**, 012331 (2005).
- [18] A. Perez-Leija, R. Keil, A. Kay, H. Moya-Cessa, S. Nolte, L.-C. Kwek, B. M. Rodríguez-Lara, A. Szameit, and D. N. Christodoulides, *Phys. Rev. A* **87**, 012309 (2013).
- [19] R. J. Chapman, M. Santandrea, Z. Huang, G. Corrielli, A. Crespi, M.-H. Yung, R. Osellame, and A. Peruzzo, *Nat. Comm.* **7**, 11339 (2016).
- [20] J. M. Chow, A. D. Córcoles, J. M. Gambetta, C. Rigetti, B. R. Johnson, J. A. Smolin, J. R. Rozen, G. A. Keefe, M. B. Rothwell, M. B. Ketchen, et al., *Phys. Rev. Lett.* **107**, 080502 (2011).
- [21] S. Poletto, J. M. Gambetta, S. T. Merkel, J. A. Smolin, J. M. Chow, A. D. Córcoles, G. A. Keefe, M. B. Rothwell, J. R. Rozen, D. W. Abraham, et al., *Phys. Rev. Lett.* **109**, 240505 (2012).
- [22] L. DiCarlo, J. M. Chow, J. M. Gambetta, L. S. Bishop, B. R. Johnson, D. I. Schuster, J. Majer, A. Blais, L. Frunzio, S. M. Girvin, et al., *Nature* **460**, 240 (2009).
- [23] J. Kelly, R. Barends, A. G. Fowler, A. Megrant, E. Jeffrey, T. C. White, D. Sank, J. Y. Mutus, B. Campbell, Y. Chen, et al., *Nature* **519**, 66 (2015).
- [24] A. Niskanen, K. Harrabi, F. Yoshihara, Y. Nakamura, S. Lloyd, and J. Tsai, *Science* **316**, 723 (2007).
- [25] D. C. McKay, S. Filipp, A. Mezzacapo, E. Magesan, J. M. Chow, and J. M. Gambetta, *Phys. Rev. A* **6**, 064007 (2016).
- [26] R. Naik, N. Leung, S. Chakram, P. Groszkowski, Y. Lu, N. Earnest, D. McKay, J. Koch, and D. Schuster, *Nat. Comm.* **8**, 1904 (2017).
- [27] Y. Lu, S. Chakram, N. Leung, N. Earnest, R. K. Naik, Z. Huang, P. Groszkowski, E. Kapit, J. Koch, and D. I. Schuster, *Phys. Rev. Lett.* **119**, 150502 (2017).
- [28] Q. M. Chen, R. B. Wu, L. Sun, and Y. X. Liu, arXiv:1712.04357 (2017).
- [29] C. Neill, P. Roushan, K. Kechedzhi, S. Boixo, S. Isakov, V. Smelyanskiy, A. Megrant, B. Chiaro, A. Dunsworth, K. Arya, et al., *Science* **360**, 195 (2018).
- [30] J. Strand, M. Ware, F. Beaudoin, T. Ohki, B. Johnson, A. Blais, and B. Plourde, *Phys. Rev. B* **87**, 220505 (2013).
- [31] Y. X. Liu, C. X. Wang, H. C. Sun, and X. B. Wang, *New J. Phys.* **16**, 015031 (2014).
- [32] Y. Wu, L. Yang, Y. Zheng, H. Deng, Z. Yan, Y. Zhao, K. Huang, W. J. Munro, K. Nemoto, D. Zheng, et al., arXiv:1605.06747 (2016).
- [33] S. Caldwell, N. Didier, C. A. Ryan, E. A. Sete, A. Hudson, P. Karalekas, R. Manenti, M. Reagor, M. P. da Silva, R. Sinclair, et al., arXiv:1706.06562 (2017).
- [34] M. Reagor, C. B. Osborn, N. Tezak, A. Staley, G. Prawiroatmodjo, M. Scheer, N. Alidoust, E. A. Sete, N. Didier, M. P. da Silva, et al., *Sci. Adv.* **4**, eaao3603 (2018).
- [35] A. A. Houck, H. E. Türeci, and J. Koch, *Nat. Phys.* **8**, 292 (2012).
- [36] I. M. Georgescu, S. Ashhab, and F. Nori, *Rev. Mod. Phys.* **86**, 153 (2014).
- [37] Supplementary Materials.
- [38] J. Clarke and F. K. Wilhelm, *Nature* **453**, 1031 (2008).
- [39] J. Q. You and F. Nori, *Nature* **474**, 589 (2011).
- [40] M. H. Devoret and R. J. Schoelkopf, *Science* **339**, 1169 (2013).
- [41] R. Barends, J. Kelly, A. Megrant, D. Sank, E. Jeffrey, Y. Chen, Y. Yin, B. Chiaro, J. Mutus, C. Neill, et al., *Phys. Rev. Lett.* **111**, 080502 (2013).
- [42] R. Barends, J. Kelly, A. Megrant, A. Veitia, D. Sank, E. Jeffrey, T. C. White, J. Mutus, A. G. Fowler, B. Campbell, et al., *Nature* **508**, 500 (2014).
- [43] M. Hatridge, R. Vijay, D. H. Slichter, J. Clarke, and I. Siddiqi, *Phys. Rev. B* **83**, 134501 (2011).
- [44] T. Roy, S. Kundu, M. Chand, A. M. Vadiraj, A. Ranadive, N. Nehra, M. P. Patankar, J. Aumentado, A. A. Clerk, and R. Vijay, *Appl. Phys. Lett.* **107**, 262601 (2015).
- [45] A. Kamal, A. Marblestone, and M. H. Devoret, *Phys. Rev. B* **79**, 184301 (2009).
- [46] K. W. Murch, S. J. Weber, C. Macklin, and I. Siddiqi, *Nature* **502**, 211 (2013).
- [47] N. Didier, E. A. Sete, M. P. da Silva, and C. Rigetti, *Phys. Rev. A* **97**, 022330 (2018).
- [48] J. M. Chow, J. M. Gambetta, L. Tornberg, J. Koch, L. S. Bishop, A. A. Houck, B. R. Johnson, L. Frunzio, S. M. Girvin, and R. J. Schoelkopf, *Phys. Rev. Lett.* **102**, 090502 (2009).
- [49] F. Mei, G. Chen, L. Tian, S. Zhu, and S. Jia, arXiv:1711.07751 (2017).
- [50] N. Goldman, G. Juzeliūnas, P. Öhberg, and I. B. Spielman, *Rep. Prog. Phys.* **77**, 126401 (2014).

Supplementary Materials for “Perfect remote quantum state transfer in a superconducting qubit chain with parametrically tunable couplings”

X. Li,^{1,*} Y. Ma,^{1,*} J. Han,¹ Tao Chen,² Y. Xu,¹ W. Cai,¹ H. Wang,¹
Y. Song,¹ Zheng-Yuan Xue,^{2,†} Zhang-qi Yin,^{1,‡} and Luyan Sun^{1,§}

¹Center for Quantum Information, Institute for Interdisciplinary Information Sciences, Tsinghua University, Beijing 100084, China

²Guangdong Provincial Key Laboratory of Quantum Engineering and Quantum Materials, and School of Physics and Telecommunication Engineering, South China Normal University, Guangzhou 510006, China

TUNABLE INTERACTION

Here we present details to tune the coupling strength of two adjacent qubits in a chain of N coupled qubits. A wide range coupling tunability can be achieved through parametric modulations of the qubits $\omega_j = \omega_{oj} + \varepsilon_j \sin(\nu_j t + \varphi_j)$ with $j = 1, \dots, N - 1$. We define a rotating frame through $U = U_1 \times U_2$ with

$$U_1 = \exp \left[-i \left(\frac{\omega_0}{2} \sigma_0^z + \sum_{j=1}^{N-1} \frac{\omega_{oj}}{2} \sigma_j^z \right) t \right] \quad (1)$$

and

$$U_2 = \exp \left[i \sum_{j=1}^{N-1} \sigma_j^z \frac{\alpha_j}{2} \cos(\nu_j t + \varphi_j) \right], \quad (2)$$

where $\alpha_j = \varepsilon_j / \nu_j$. In this rotating frame, the transformed Hamiltonian is

$$\begin{aligned} H_I &= U^\dagger H U + i \frac{dU^\dagger}{dt} U \\ &= g_1 \sigma_0^+ \sigma_1^- e^{-i\Delta_1 t} \exp[i\alpha_1 \cos(\nu_1 t + \varphi_1)] \\ &\quad + \sum_{j=2}^{N-1} g_j \sigma_{j-1}^+ \sigma_j^- \exp[-i\alpha_{j-1} \cos(\nu_{j-1} t + \varphi_{j-1})] \\ &\quad \times \exp[i\alpha_j \cos(\nu_j t + \varphi_j) - i\Delta_j t] + \text{H.c.} \end{aligned} \quad (3)$$

When $\Delta_j = \omega_{oj} - \omega_{o(j-1)}$ equals to ν_j ($-\nu_j$) for odd (even) j , using the Jacobi-Anger identity

$$\exp[i\alpha \cos(\nu t + \varphi)] = \sum_{m=-\infty}^{\infty} i^m J_m(\alpha) \exp[im(\nu t + \varphi)]$$

and applying the rotating-wave approximation by neglecting the high-order oscillating terms, the effective tunable resonant qubit-qubit interaction becomes Eq. (3) in the main text.

EXPERIMENTAL DEVICE

Fabrication of the experimental device includes the following six main steps. (1) A 100 nm aluminum film is deposited directly onto a two-inch c -plane sapphire wafer in Plassys MEB 550S without any pre-cleaning treatment. (2) E-beam lithography followed by an evaporation of gold

is to create alignment marks for the subsequent lithography steps. (3) Photo-lithography followed by inductively coupled plasma etching is used to define transmission line, readout resonators, control lines, and large pads of the Xmon qubits. (4) Josephson junctions are fabricated with E-beam lithography and double-angle evaporations of aluminum in Plassys MEB 550S. (5) The wafer is then diced into 7 mm by 7 mm chips. (6) The selected chip is wire bonded in an aluminum box without printed circuit board for a final packaging before measurement. We apply on-chip bonding-wire crossovers as many as possible to reduce the impact of the parasitic modes.

Our sample is measured in a dilution refrigerator with a base temperature about 10 mK. Details of our measurement circuitry are shown in Fig. S1. For full manipulation of four qubits, we use two four-channel arbitrary waveform generators (AWG). One AWG provides two pairs of sideband modulations for XY control and readout of the qubits respectively. The second AWG, synchronized with the first one, is to realize individual Z control of the qubits. The XY control signals are generated from a single microwave generator modulated with different sideband frequencies. This way of control guarantees stable phase differences among the four qubits during the quantum state transfer (QST) experiment. The readout signals for individual qubits are realized in a similar way to make sure that the phases of the final demodulated readout signals are fixed for each run. A Josephson parametric amplifier (JPA) [1–4] at 10 mK with a gain over 20 dB and a bandwidth about 260 MHz is used as the first stage of amplification, allowing for high-fidelity single-shot measurements of the qubits. Its gain profile is shown in Fig. S2.

Readout resonator frequencies, qubit frequencies, qubit coherence times, coupling strengths, and readout resonator decay rates are all presented in Table I. The readout frequencies of the four qubits span a range of about 60 MHz, well within the bandwidth of the JPA. In the current device, the dispersive shifts χ_{qr} (between each qubit and its readout resonator) and the readout resonator decay rates κ_r are not matched for the best signal-to-noise ratio.

QUBIT READOUT PROPERTIES AND PROCESS TOMOGRAPHY

With the help of JPA, all qubits at the idle points can be readout individually with high fidelities. Figure S3 shows the readout histograms of each qubit when all other qubits are in

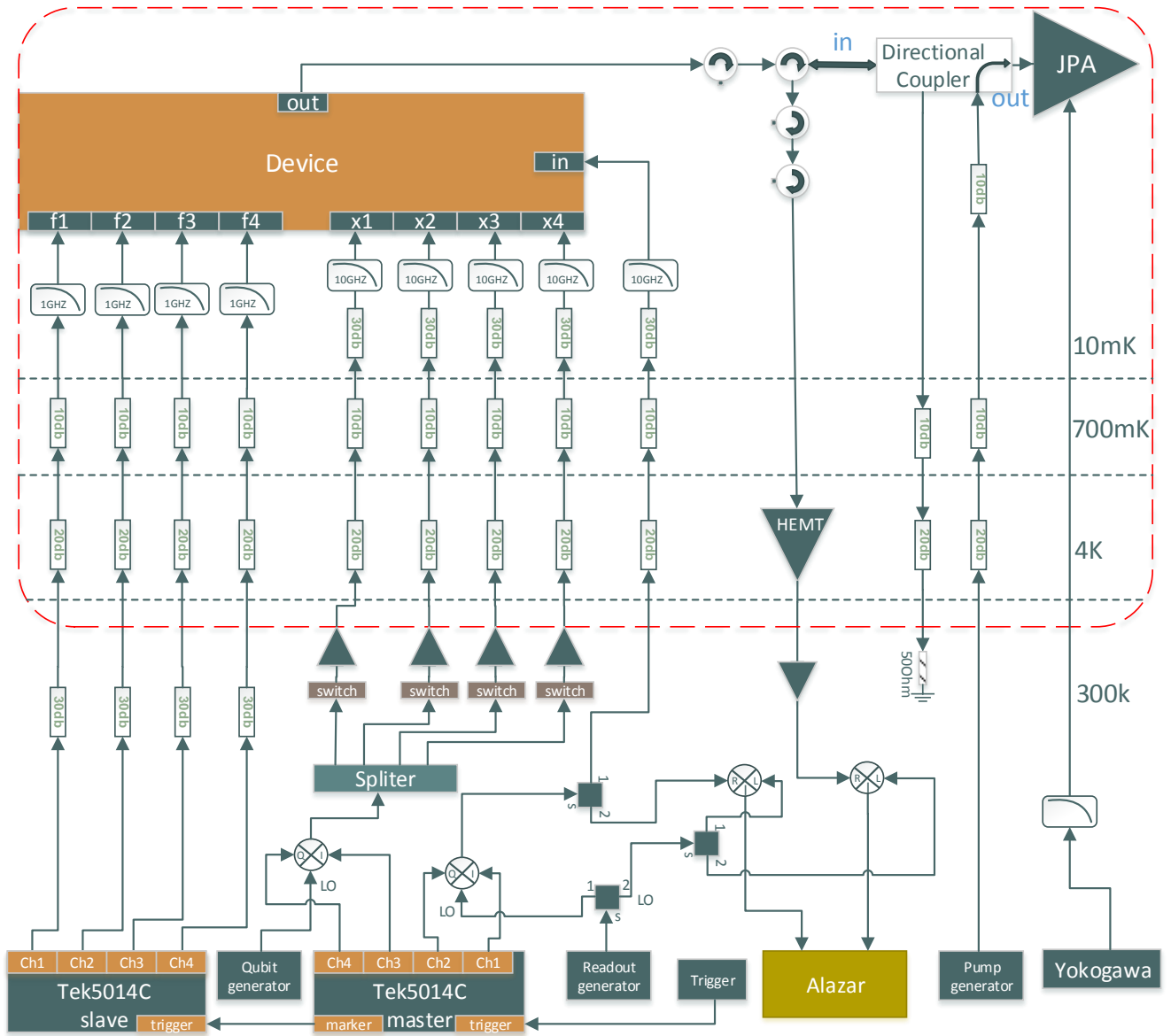


FIG. S1. Details of wiring and circuit components. The experimental device consists of five cross-shaped transmon qubits ($Xmons, Q_0 - Q_4$) [5–7] arranged in a linear array with nearly identical nearest-neighbor coupling strengths. Each qubit has independent XY and Z controls which are properly attenuated and low-pass filtered. A common transmission line is coupled to separate $\lambda/4$ resonators for individual readouts of the qubits. Two four-channel AWGs are used to fully manipulate the four qubits ($Q_0 - Q_3$) to realize the QST. The fifth qubit Q_4 is biased with a DC source at a low frequency (< 4 GHz) and is nearly completely decoupled from the first four qubits. The “master” AWG provides two pairs of sideband modulations at different frequencies, in combination with a qubit generator and a readout generator as local oscillators (LO), allowing for XY control and readout of the qubits respectively. The XY control signal is divided by a 4-way power divider, and the outputs are connected to the respective qubit XY control lines through separate RF switches. These switches provide selective control of individual qubits. The “slave” AWG, triggered by the master one, is used to achieve Z control of the qubits through individual flux-bias lines. A JPA at 10 mK with a gain over 20 dB and a bandwidth about 260 MHz is used as the first stage of amplification, allowing for high-fidelity single-shot measurements of the qubits. A high-electron-mobility-transistor (HEMT) amplifier at 4 K and an amplifier at room temperature are also used before the down-conversion of the readout signal to the applied sideband frequencies with the same readout generator as LO. Part of the readout signal does not go through the dilution refrigerator and is used as a reference to lock the phase of the returning readout signal from the device for a better measurement stability.

their thermal steady states. Due to the mismatch of the dispersive shift and the readout resonator decay rate, the two Gaussians in the histograms corresponding to the ground state $|g\rangle$ and the excited state $|e\rangle$ are not perfectly separated. The read-

out fidelities F_g and F_e for each qubit are listed in Table II. Here F_g is measured for an initial thermal steady state, while F_e corresponds to an initial thermal steady state followed by the corresponding π rotation. The infidelity of F_g mainly

TABLE I. **Device parameters.** The parameters associated with qubit Q_4 are not presented since it is not involved in the QST experiment.

Parameters	Q_0	Q_1	Q_2	Q_3
Readout frequency (GHz)	6.8389	6.8636	6.8794	6.9014
Qubit frequency (GHz) (sweet spot)	4.8354	5.1802	4.9169	5.1916
T_1 (μ s) (sweet spot)	22.2	18.5	25.1	23.4
T_2^* (μ s) (sweet spot)	23.3	26.5	17.3	10.3
T_{2E} (μ s) (sweet spot)	24.0	41.1	29.3	32.2
T_1 (μ s) (operating point)	17.5	21.1	19.8	18.0
T_2^* (μ s) (operating point)	6.1	4.3	4.8	3.3
neighboring qubit coupling strength $g_j/2\pi$ (MHz)		16.68	17.50	17.52
qubit-readout dispersive shift $\chi_{qr}/2\pi$ (MHz)	0.17	0.26	0.2	0.2
readout resonator decay rate $\kappa_r/2\pi$ (MHz)	0.88	1.06	1.23	0.88

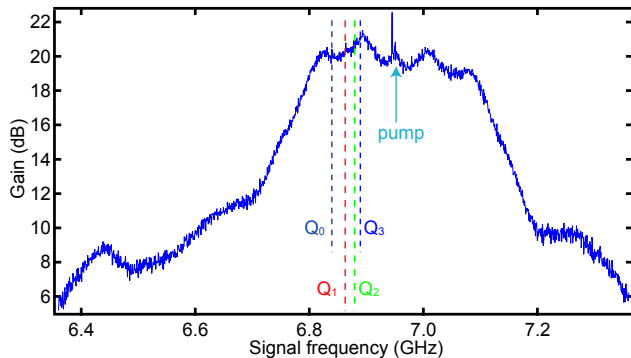


FIG. S2. **Gain profile of the JPA.** The JPA is single-pumped at a frequency of 6.951 GHz. The dashed lines represent the readout frequencies for Q_0 - Q_3 respectively. The maximum gain is larger than 20 dB and the bandwidth is about 260 MHz.

comes from the thermal population of the qubit (about 0.02 on average from an independent measurement) and the Gaussian tail after thresholding. The lower value of F_e is dominantly due to an extra decay during the measurement time, 2μ s in our experiment. To overcome these imperfections, we use a calibration matrix to reconstruct the readout results based on Bayes' rule.

For the j th qubit, we have the calibration matrix

$$F_{Qj} = \begin{pmatrix} F_{gj} & 1 - F_{ej} \\ 1 - F_{gj} & F_{ej} \end{pmatrix}.$$

The final state population of the qubit as a column vector P_{fj} can be reconstructed from the measured population P_{mj} based on the inverse of the calibration matrix

$$P_{fj} = F_{Qj}^{-1} \cdot P_{mj}.$$

We note that due to residual ZZ coupling (which depends on the detuning) between qubits, histograms of each qubit are slightly shifted when the other qubits are not in their thermal steady states. In this case, more thorough calibrations are needed in order to get better calibration matrices. We contribute the imperfect readout calibration matrices to the deviation between experiment and simulation (Fig. 3b in the main

TABLE II. **The readout fidelities for each qubit.** The fidelities are based on the histograms presented in Fig. S3. F_g is measured for an initial thermal steady state. F_e corresponds to an initial thermal steady state followed by the corresponding π rotation.

	Q_0	Q_1	Q_2	Q_3
F_{gj}	0.963	0.951	0.942	0.939
F_{ej}	0.898	0.869	0.869	0.858

text). However, after a perfect QST (Fig. 4d in the main text), the tomography measurement of Q_3 does not have this issue since all other three qubits have returned to their initial states.

Process tomography is realized by preparing four linear independent initial states $\{|g\rangle, |e\rangle, (|g\rangle + |e\rangle)/\sqrt{2}, (|g\rangle - i|e\rangle)/\sqrt{2}\}$ on Q_0 , and performing the corresponding final state tomography of Q_3 after the QST. Based on these processes, we derive the 4×4 process matrix χ_M [8, 9]. The fidelity is defined as the overlap between χ_M and χ_{ideal} (χ_{ideal} is for a perfect QST) $F = \text{tr}(\chi_M \chi_{ideal})$.

CROSSTALK AND DECONVOLUTION OF FLUX BIAS LINE

Due to the ground plane return currents, there are inevitable crosstalks (the maximum one in our device is about 10%) between flux-bias lines and qubits. That is, changing the bias on any single qubit's flux line actually changes all of the qubit frequencies. However, this crosstalk can be corrected by orthogonalization of the flux-bias lines [10]. For each qubit, we measure its frequency change as a function of the applied voltage on each flux bias line. For small voltages, the frequency dependence is approximately linear. Therefore, the ratios among the slopes represent the relative coupling strengths between the flux-bias lines and the specific qubit. By combing the results from all four qubits, we can get the qubit frequency response matrix M_z . The inverse of M_z gives the orthogonalization matrix \widetilde{M}_z which allows for independent control of only the desired qubit without changing the other qubit frequencies:

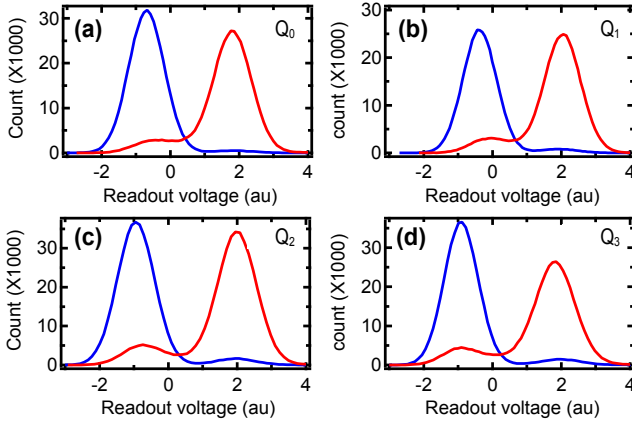


FIG. S3. **Readout histograms.** (a)-(d) Histograms for Q_0 - Q_3 respectively. Each histogram is measured separately with a total count of 90,000, while the other qubits are in their thermal steady states. Blue curves are for an initial thermal steady state and red curves are for an initial thermal steady state followed by the corresponding π rotation.

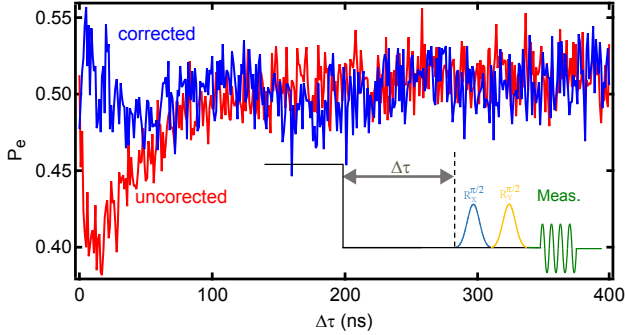


FIG. S4. **Qubit response to fast flux bias.** The red curve corresponds to the uncorrected response. The blue curve corresponds to the corrected response after deconvolution. The inset shows the pulse sequence of the experiment.

$$\widetilde{M}_z = M_z^{-1} = \begin{pmatrix} 0.9934 & 0.0822 & 0.021 & 0.0158 \\ -0.0714 & 0.9843 & 0.0595 & 0.0361 \\ -0.0222 & -0.1278 & 0.9888 & 0.074 \\ -0.0087 & -0.057 & -0.0414 & 0.9447 \end{pmatrix}.$$

To achieve a high-fidelity QST, flux-bias lines in fast time scales are also necessary to be carefully calibrated to compensate for the finite rise time and ringing of the flux-control pulses. These flux-bias imperfections, seen by the qubit,

mainly come from the control circuit including the AWG to generate those control pulses, wiring outside and inside the refrigerator. We use the deconvolution method to correct the unwanted response in the control system based on the measured response function of the control circuit [11]. The performance of this correction can be verified by a measurement of the qubit response to a step pulse on the flux bias based on a sequence shown in the inset of Fig. S4 [12]. The results shown in Fig. S4 indeed demonstrate an improvement after correction.

* These two authors contributed equally to this work.

† zyxue83@163.com

‡ yinzhangqi@tsinghua.edu.cn

§ luyansun@tsinghua.edu.cn

- [1] M. Hatridge, R. Vijay, D. H. Slichter, J. Clarke, and I. Siddiqi, *Phys. Rev. B* **83**, 134501 (2011).
- [2] T. Roy, S. Kundu, M. Chand, A. M. Vadiraj, A. Ranadive, N. Nehra, M. P. Patankar, J. Aumentado, A. A. Clerk, and R. Vijay, *Appl. Phys. Lett.* **107**, 262601 (2015).
- [3] A. Kamal, A. Marblestone, and M. H. Devoret, *Phys. Rev. B* **79**, 184301 (2009).
- [4] K. W. Murch, S. J. Weber, C. Macklin, and I. Siddiqi, *Nature* **502**, 211 (2013).
- [5] R. Barends, J. Kelly, A. Megrant, D. Sank, E. Jeffrey, Y. Chen, Y. Yin, B. Chiaro, J. Mutus, C. Neill, P. O'Malley, P. Roushan, J. Wenner, T. C. White, A. N. Cleland, and J. M. Martinis, *Phys. Rev. Lett.* **111**, 080502 (2013).
- [6] R. Barends, J. Kelly, A. Megrant, A. Veitia, D. Sank, E. Jeffrey, T. C. White, J. Mutus, A. G. Fowler, B. Campbell, Y. Chen, Z. Chen, B. Chiaro, A. Dunsworth, C. Neill, P. O'Malley, P. Roushan, A. Vainsencher, J. Wenner, A. N. Korotkov, A. N. Cleland, and J. M. Martinis, *Nature* **508**, 500 (2014).
- [7] J. Kelly, R. Barends, A. G. Fowler, A. Megrant, E. Jeffrey, T. C. White, D. Sank, J. Y. Mutus, B. Campbell, Y. Chen, Z. Chen, B. Chiaro, A. Dunsworth, I.-C. Hoi, C. Neill, P. J. J. O'Malley, C. Quintana, P. Roushan, A. Vainsencher, J. Wenner, A. N. Cleland, and J. M. Martinis, *Nature* **519**, 66 (2015).
- [8] M. A. Nielsen and I. L. Chuang, *Quantum Computation and Quantum Information* (Cambridge Univ. Press, 2000).
- [9] J. M. Chow, J. M. Gambetta, L. Tornberg, J. Koch, L. S. Bishop, A. A. Houck, B. R. Johnson, L. Frunzio, S. M. Girvin, and R. J. Schoelkopf, *Phys. Rev. Lett.* **102**, 090502 (2009).
- [10] M. D. Reed, *Entanglement and Quantum Error Correction with Superconducting Qubits*, Ph.D. thesis, Yale University (2013).
- [11] B. R. Johnson, *Controlling Photons in Superconducting Electrical Circuits*, Ph.D. thesis, Yale University (2010).
- [12] J. S. Kelly, *Fault-Tolerant Superconducting Qubits*, Ph.D. thesis, University of California, Santa Barbara (2015).